

# An *ab-initio* calculation of magnetic resonant x-ray scattering spectra in NiO

Manabu Usuda, \*Manabu Takahashi, and Jun-ichi Igarashi

Synchrotron Radiation Research Center, Japan Atomic Energy Research Institute, Hyogo 679-5148, Japan

\*Faculty of Engineering, Gunma University, Kiryu, Gunma 376-8515, Japan

(Dated: October 29, 2018)

We investigate the magnetic resonant x-ray scattering spectra around the  $K$  edge of Ni in antiferromagnetic NiO using an *ab-initio* band-structure calculation based on the density-functional theory. By taking account of orbital polarization through the spin-orbit interaction, we reproduce well the spectra obtained experimentally, thus demonstrating the usefulness of the *ab-initio* calculation. It is shown that the main-edge peak, which mainly comes from the dipolar ( $1s \rightarrow 4p$ ) transition, is a direct reflection of the orbital polarization of the  $4p$  states. It is clarified that the  $4p$  orbital polarization is mainly induced from the spin polarization on the  $4p$  states by the spin-orbit interaction. The  $3d$  orbital polarization at neighboring Ni sites gives rise to only a minor contribution to the  $4p$  orbital polarization through a  $p$ - $d$  mixing. It is also shown that the pre-edge peak, which mainly originates from the quadrupolar ( $1s \rightarrow 3d$ ) transition, is a direct reflection of the orbital polarization of the unoccupied  $3d$  states. It shows a Fano-type antiresonant dip due to interference with the nonresonant contribution, in agreement with the experimental result.

PACS numbers: 78.70.Ck, 71.20.Be, 75.50.Ee

## I. INTRODUCTION

Resonant x-ray scattering (RXS) is a powerful tool for investigating the properties of magnetic and orbital orders. Resonant enhancements on antiferromagnetic (AF) superlattice spots have been observed in several transition-metal compounds such as  $\text{RbMnF}_3$  (Ref. 1),  $\text{KCuF}_3$  (Ref. 2),  $\text{CoO}$  (Ref. 3) and  $\text{NiO}$  (Refs. 4,5). RXS is described as a second-order process wherein a photon is virtually absorbed upon exciting a core electron to unoccupied states, and then emitted upon recombining the excited electron with the core hole. For the  $3d$  transition-metal  $K$ -edge, the intermediate states involve unoccupied  $4p$  states in the dipolar (E1) transition and unoccupied  $3d$  states in the quadrupolar (E2) transition. The RXS intensities due to the E1 and E2 transitions constitute main-edge and pre-edge structures, respectively. The main-edge intensity is sensitive to the electronic structure of neighboring sites since the unoccupied  $4p$  states are highly extended in space. This characteristic is now well recognized in RXS on orbital superlattice spots in the  $K$  edge of transition-metal compounds. At an early stage, a mechanism was proposed, according to which the intensity is related to the  $4p$  states modified by the intra-atomic Coulomb interaction with the  $3d$  electrons constituting the orbital order<sup>6,7</sup>, but extensive studies based on band-structure calculations<sup>8,9,10</sup> revealed that the intensity is related to the  $4p$  states modified by the lattice distortion.

In our previous work,<sup>11</sup> we studied the mechanism of magnetic RXS in the antiferromagnetic phase of  $\text{NiO}$ , and analyzed the experiment performed by Neubeck *et al.*<sup>5</sup> To deal with the extended nature of the  $4p$  states, we used a tight-binding model. Since orbitals must couple to the magnetic order to generate the intensity of the magnetic RXS, it is essential to take account of the spin-orbit interaction (SOI). The spin polarization alone in

the  $4p$  states cannot give rise to the intensity, because, if we add the amplitudes due to up-spin electrons to that due to down-spin electrons, the total becomes the same at each site, leading to a cancellation of amplitudes between different magnetic sublattices. Through the model calculation, we clarified that the main-edge intensity is generated from the orbital polarization in the  $4p$  states. Generally speaking, such polarization is brought about by the  $4p$  SOI, by the intra-atomic Coulomb interaction between the  $4p$  and  $3d$  states, and by the mixing of the  $4p$  states with the  $3d$  states of neighboring Ni atoms. Although we obtained the magnetic RXS spectra that were in qualitative agreement with the experiment, it is still unclear how the  $4p$  states are orbitally polarized. In this paper, to eliminate the uncertainty of the model calculation, and to clarify the mechanism of the magnetic RXS, we carry out an *ab-initio* calculation of the RXS spectra using a band-structure calculation based on the density-functional theory. We take account of the SOI to deal with the orbital polarization. We neglect the attractive interaction between the photoexcited electron and the  $1s$  core hole. This effect on the  $4p$  states is known to be small, from the analysis of the magnetic circular dichroism (MCD)<sup>12,13,14</sup> and of the RXS on orbital superlattice spots at the  $K$  edge of transition metals.<sup>9,10,15</sup>

In this paper, we show that the *ab-initio* calculation reproduces well the experimental spectra. Moreover, we calculate the spectra by turning the SOI on and off selectively in several states in order to clarify how the  $4p$  orbital polarization is brought about. The result is that the main-edge intensity is slightly reduced when the SOI on the  $3d$  states is turned off, while it is largely diminished when the SOI on the  $4p$  states is turned off. This indicates that the  $3d$  orbital polarization has little influence on the  $4p$  orbital polarization. The same conclusion has been drawn on the basis of an *ab-initio* calculation of the magnetic RXS spectra for  $\text{KCuF}_3$  (Ref. 15) and a

recent analysis of MCD in  $\text{Mn}_3\text{GaC}$  (Ref. 16).

We also calculate the contribution of the E2 and non-resonant processes. We obtain a single peak in the pre-edge region. It is shown to originate from the orbital polarization in the 3d states. Although the 3d orbital polarization is much larger than the 4p orbital polarization, the obtained pre-edge peak is rather small compared to the main-edge peak. The peak position is at a higher energy than the experimental one. We can ascribe this discrepancy to the neglect of the interaction between the 1s core hole and the 3d electrons in the present calculation. We also reproduce well the Fano-type antiresonant dip due to the interference between the E2 and the non-resonant contributions.

This paper is organized as follows. In Sec. II, we show the results of band-structure calculations and discuss the ground state in the antiferromagnetic phase of NiO. In Section III, we briefly describe the formulae used in calculating the magnetic RXS spectra. In Sec. IV, we present the calculated magnetic RXS spectra and compare them with experimental data. Section V is devoted to concluding remarks.

## II. ELECTRONIC STRUCTURE OF NICKEL OXIDE

NiO has the NaCl-type structure with the lattice constant of  $a = 4.177 \text{ \AA}$  (Ref. 17). Nickel atoms form an fcc lattice, as illustrated in Fig. 1. Type-II AF order develops below  $T_N = 523 \text{ K}$ . The order parameter is characterized by a wave vector  $\mathbf{Q}$ , which is directed to one of four body-diagonals in the fcc lattice. We selectively assume that  $\mathbf{Q} = (\frac{1}{2}\frac{1}{2}\frac{1}{2})$  in the present study. The magnetic moment lies in the plane perpendicular to the AF modulation direction; three directions,  $\mathbf{S}_1 = [-1, -1, 2]$ ,  $\mathbf{S}_2 = [2, -1, -1]$ , or  $\mathbf{S}_3 = [-1, 2, -1]$  can be taken for  $\mathbf{Q} = (\frac{1}{2}\frac{1}{2}\frac{1}{2})$ . Note that the experiment of the magnetic RXS in NiO has been performed under the condition that  $\mathbf{Q}$  is specified but domains are formed with respect to the spin direction<sup>5,17</sup>.

The electronic band structure of NiO is calculated using the full-potential linearized augmented-plane-wave (FLAPW) method<sup>18,19</sup> in the local-density approximation (LDA). The local exchange-correlation functional of Vosko, Wilk and Nusair<sup>20</sup> is employed. The experimental lattice constant is used and the muffin-tin (MT) radii are set to be 2.2 a.u. for nickel and 1.6 a.u. for oxygen. We also perform LDA+ $U$  calculation<sup>21,22</sup> with the effective Coulomb parameter  $U_{\text{eff}} = U - J$  for the Ni 3d states, in order to investigate the effect of the band gap and the magnetic moment on the RXS spectra.

Table I shows the calculated values of the band gap and the magnetic moments in comparison with the experiments. LDA calculation considerably underestimates the magnetic moment and band gap magnitudes. Introducing  $U_{\text{eff}}$  enhances them but the obtained magnitudes are still smaller than those in the experiments.

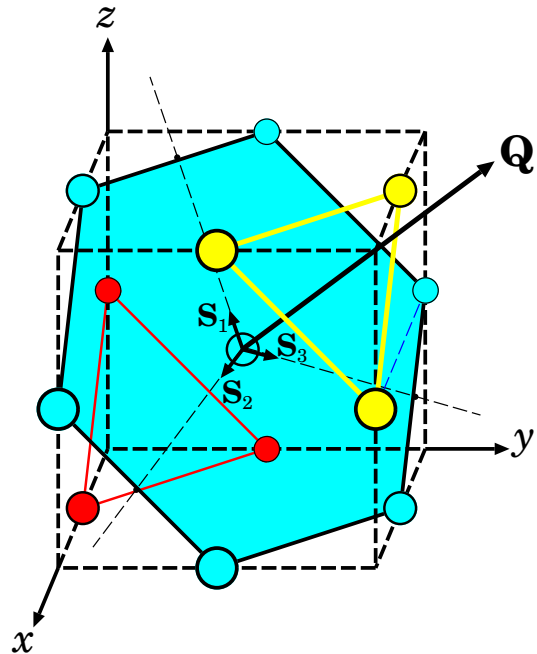


FIG. 1: Sketch of a NiO crystal (only Ni atoms are shown). Wave vector  $\mathbf{Q} = (\frac{1}{2}\frac{1}{2}\frac{1}{2})$  characterizes an antiferromagnetic modulation direction. Three arrows denoted as  $\mathbf{S}_1$ ,  $\mathbf{S}_2$ ,  $\mathbf{S}_3$ , in a plane perpendicular to  $\mathbf{Q}$  indicate possible spin directions ( $S$  domains). Spins for solid, gray, and open circles align alternately.

TABLE I: Calculated band gap and magnetic moments, compared with those in the experiments.  $2S$  and  $L$  are spin and orbital moments, respectively. In the LDA+ $U$  calculations, the effective parameters of (1)  $U_{\text{eff}} = 2 \text{ eV}$  and (2)  $U_{\text{eff}} = 5 \text{ eV}$  are employed.

	$E_{\text{gap}} [\text{eV}]$	$2S [\hbar]$	$L [\hbar]$	$L + 2S [\hbar]$	$L/S$
LDA	0.408	1.210	0.151	1.361	0.25
LDA+ $U$ (1)	1.438	1.467	0.187	1.654	0.25
LDA+ $U$ (2)	2.839	1.647	0.233	1.880	0.28
Exp. <sup>a</sup>	4.3 <sup>b</sup>	1.88	0.32	2.20, 1.90 <sup>c</sup>	0.34

<sup>a</sup>Unless noted, Ref. 23.

<sup>b</sup>Reference 24.

<sup>c</sup>Reference 25.

Figure 2 shows the density of states (DOS) projected on the  $p$  and  $d$  symmetric states inside the MT sphere at a Ni site, calculated in the LDA. The origin of the energy is set at the top of the valence band. The right part of the figure is shown on a 20-times magnified scale. The  $p$  and  $d$  symmetric states are sometimes referred to as the 4p and 3d states, respectively, because the wave functions are similar to atomic 4p and 3d wave functions inside the MT sphere. The magnitude of the 4p DOS is much smaller than that of the 3d DOS, because most of the 4p density is distributed over the interstitial region or on neighboring sites. Introducing large  $U_{\text{eff}}$ , such as  $U_{\text{eff}} = 5 \text{ eV}$ , in the LDA+ $U$  calculation considerably changes the 3d DOS

(not shown), while the 4p DOS remains almost the same. Also, exchange splitting in the 4p DOS is negligibly small in contrast with the large exchange splitting in the 3d states. Both observations suggest that the effect of the 3d states on the 4p states is very small.

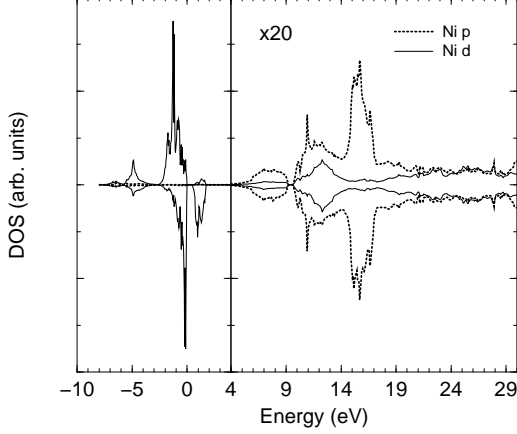


FIG. 2: Projected density of states of the Ni 3d and 4p states calculated in the LDA. All energies are given with respect to the top of the valence band.

### III. FORMULATION FOR MAGNETIC RXS

We consider the situation that a photon with the energy  $\hbar\omega$ , the momentum  $\mathbf{k}_i$ , and the polarization  $\mu$  ( $= \sigma$  or  $\pi$ ) with the polarization vector  $\hat{\epsilon}$ , is scattered into the state with the same energy  $\hbar\omega$  (elastic scattering), the momentum  $\mathbf{k}_f$ , and the polarization  $\mu'$  ( $= \sigma'$  or  $\pi'$ ) with the polarization vector  $\hat{\epsilon}'$ . The scattering geometry is depicted in Fig. 3. The magnetic scattering amplitude is derived from Fermi's golden rule to the second order<sup>26,27,28,29,30,31</sup>, in which the amplitude consists of resonant and nonresonant scatterings. We consider the resonant E1 and E2 transitions and the nonresonant contribution. The cross section for the elastic scattering at a magnetic superlattice spot is expressed as

$$\frac{d\sigma}{d\Omega} \propto |T_{\mu \rightarrow \mu'}(\mathbf{G}, \omega) + J_{\mu \rightarrow \mu'}(\mathbf{G}, \omega) + L_{\mu \rightarrow \mu'}(\mathbf{G}, \omega)|^2, \quad (1)$$

where  $\mathbf{G} = \mathbf{k}_f - \mathbf{k}_i$  is a scattering vector.

The nonresonant term  $T_{\mu \rightarrow \mu'}(\mathbf{G}, \omega)$  is given by

$$T_{\mu \rightarrow \mu'}(\mathbf{G}, \omega) = -\frac{i\hbar\omega}{mc^2} \left( \frac{1}{2} \mathbf{L}(\mathbf{G}) \cdot \mathbf{A}'' + \mathbf{S}(\mathbf{G}) \cdot \mathbf{B} \right), \quad (2)$$

where  $m$  is the electron mass and  $c$  is the light velocity. The vectors  $\mathbf{A}''$  and  $\mathbf{B}$  are given by

$$\mathbf{A}'' = \mathbf{A}' - (\mathbf{A}' \cdot \hat{\mathbf{G}})\hat{\mathbf{G}}, \quad \mathbf{A}' = -4 \sin^2 \theta (\hat{\epsilon}' \times \hat{\epsilon}), \quad (3)$$

$$\begin{aligned} \mathbf{B} = & \hat{\epsilon}' \times \hat{\epsilon} + (\hat{\mathbf{k}}_f \times \hat{\epsilon}')(\hat{\mathbf{k}}_f \cdot \hat{\epsilon}) - (\hat{\mathbf{k}}_i \times \hat{\epsilon})(\hat{\mathbf{k}}_i \cdot \hat{\epsilon}') \\ & - (\hat{\mathbf{k}}_f \times \hat{\epsilon}') \times (\hat{\mathbf{k}}_i \times \hat{\epsilon}), \end{aligned} \quad (4)$$

where  $\hat{\mathbf{k}}_i = \mathbf{k}_i/|\mathbf{k}_i|$ ,  $\hat{\mathbf{k}}_f = \mathbf{k}_f/|\mathbf{k}_f|$ , and  $\hat{\mathbf{G}} = \mathbf{G}/|\mathbf{G}|$ . The quantities  $\mathbf{S}(\mathbf{G})$  and  $\mathbf{L}(\mathbf{G})$  in Eq.(2) are the Fourier transforms of the spin and orbital densities, respectively<sup>31</sup>. Their approximate forms for calculation are given in the next section.

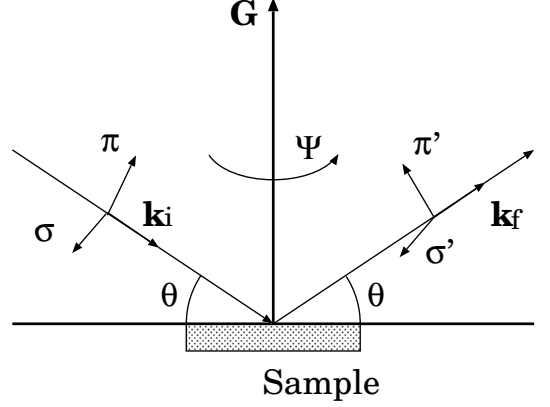


FIG. 3: Geometry of x-ray scattering. Incident photon with wave vector  $\mathbf{k}_i$  and polarization  $\sigma$  or  $\pi$  is scattered into the state with wave vector  $\mathbf{k}_f$  and polarization  $\sigma'$  or  $\pi'$  at Bragg angle  $\theta$ . The sample crystal is rotated by azimuthal angle  $\psi$  around scattering vector  $\mathbf{G} = \mathbf{k}_f - \mathbf{k}_i$ .

The resonant contribution from the E1 transition is given by

$$J_{\mu \rightarrow \mu'}(\mathbf{G}, \omega) = \sum_{\alpha\alpha'} (P^{\mu\mu'})_{\alpha} M_{\alpha\alpha'}(\mathbf{G}, \omega) P_{\alpha'}^{\mu}, \quad (5)$$

with

$$\begin{aligned} M_{\alpha\alpha'}(\mathbf{G}, \omega) &= \frac{1}{\sqrt{N}} \sum_{n,\Lambda} e^{-i\mathbf{G} \cdot \mathbf{R}_n} \frac{m\omega_{\Lambda g}^2 \langle g|x_{\alpha}(n)|\Lambda\rangle \langle \Lambda|x_{\alpha'}(n)|g\rangle}{\hbar\omega - \omega_{\Lambda g} + i\Gamma}, \end{aligned} \quad (6)$$

where  $\omega_{\Lambda g} = (E_{\Lambda} - E_g)/\hbar$ . This represents a second-order process wherein a photon is virtually absorbed upon exciting the 1s electron to the 4p states and then emitted upon recombining the excited electron with the 1s core hole. The geometrical factors  $P^{\mu}$ ,  $P^{\mu'}$  are explicitly written in the Appendix of Ref. 11.  $E_g$  represents the ground-state energy. The intermediate state  $|\Lambda\rangle$  consists of an excited electron on the 4p states and a hole on the 1s state with energy  $E_{\Lambda}$ .  $N$  represents the number of Ni sites, and  $n$  is the index for the Ni sites. The dipole operators  $x_{\alpha}(n)$  at site  $n$  are defined as  $x_1(n) = x$ ,  $x_2(n) = y$ ,  $x_3(n) = z$  in the coordinate frame fixed to the crystal axes with the origin located at the center of site  $n$ . Note that the amplitudes on magnetic spot  $\mathbf{G} = (\frac{\hbar}{2} \frac{k}{2} \frac{\ell}{2})$  are nearly canceled out between different magnetic sublattices. Only small values remain in an antisymmetric

form,

$$M(\mathbf{G}, \omega) = \begin{pmatrix} 0 & a & c \\ -a & 0 & b \\ -c & -b & 0 \end{pmatrix}, \quad (7)$$

with  $a$ ,  $b$ , and  $c$  being some complex numbers.

The resonant contribution from the E2 transition is given by

$$L_{\mu \rightarrow \mu'}(\mathbf{G}, \omega) = \sum_{\gamma \gamma'} (Q'^{\mu'})_{\gamma} N_{\gamma \gamma'}(\mathbf{G}, \omega) Q_{\gamma'}^{\mu}, \quad (8)$$

with

$$N_{\gamma \gamma'}(\mathbf{G}, \omega) = \frac{1}{\sqrt{N}} \sum_{n, \Lambda'} e^{-i\mathbf{G} \cdot \mathbf{R}_n} \times \frac{1}{12} \left( \frac{\omega}{c} \right)^2 \frac{m \omega_{\Lambda'g}^2 \langle g | z_{\gamma}(n) | \Lambda' \rangle \langle \Lambda' | z_{\gamma'}(n) | g \rangle}{\hbar \omega - \omega_{\Lambda'g} + i\Gamma}, \quad (9)$$

where  $\omega_{\Lambda'g} = (E_{\Lambda'} - E_g)/\hbar$ . The geometrical factors  $Q^{\mu}$ ,  $Q'^{\mu'}$  are given in the Appendix of Ref. 11. The intermediate states  $|\Lambda'\rangle$  consist of an excited electron on the  $3d$  states and a hole on the  $1s$  state with energy  $E_{\Lambda'}$ . The quadrupole operators  $z_{\mu}(n)$  are defined as  $z_1(n) = (\sqrt{3}/2)(x^2 - y^2)$ ,  $z_2(n) = (1/2)(3z^2 - r^2)$ ,  $z_3(n) = \sqrt{3}yz$ ,  $z_4(n) = \sqrt{3}zx$ ,  $z_5(n) = \sqrt{3}xy$ . Similar to the E1 transition, the amplitudes on magnetic spot  $\mathbf{G} = (\frac{\hbar}{2} \frac{k}{2} \frac{\ell}{2})$  are nearly canceled out between different magnetic sublattices, resulting in an antisymmetric form,

$$N(\mathbf{G}, \omega) = \begin{pmatrix} 0 & d & e & f & g \\ -d & 0 & u & p & q \\ -e & -u & 0 & r & s \\ -f & -p & -r & 0 & t \\ -g & -q & -s & -t & 0 \end{pmatrix}, \quad (10)$$

with  $d \sim u$  being some complex numbers.

#### IV. MAGNETIC RXS SPECTRA

##### A. Absorption coefficient

The absorption coefficient within the E1 transition is given by

$$A(\omega) \propto \sum_{\Lambda, \alpha} |\langle \Lambda | x_{\alpha}(j) | g \rangle|^2 \frac{\Gamma}{(\hbar \omega - E_{\Lambda})^2 + \Gamma^2}. \quad (11)$$

We neglect the core-hole potential working on the  $4p$  states in the final state of the absorption process, and replace  $|\Lambda\rangle$  by the unoccupied  $4p$  states given by the band-structure calculation. The transition matrix elements are evaluated using the LDA wave-functions. The core-hole energy is adjusted such that the calculated peak-position

coincides with the experimental one ( $\hbar \omega = 8347$  eV for the peak<sup>3</sup>). We set the core-hole lifetime width  $\Gamma$  as 1 eV. Figure 4 shows the calculated results and those of the  $K$ -edge fluorescence experiment.<sup>5</sup> The experimental spectral shape is reproduced well, suggesting that the core-hole potential plays only a minor role in the spectral shape. As already mentioned in Sec. I, this observation is consistent with the recent analysis of the  $K$ -edge MCD spectra of  $\text{Mn}_3\text{GaC}$  (Ref. 16) as well as of  $K$ -edge RXS on orbital superlattice spots in transition-metal compounds.<sup>9,10</sup>

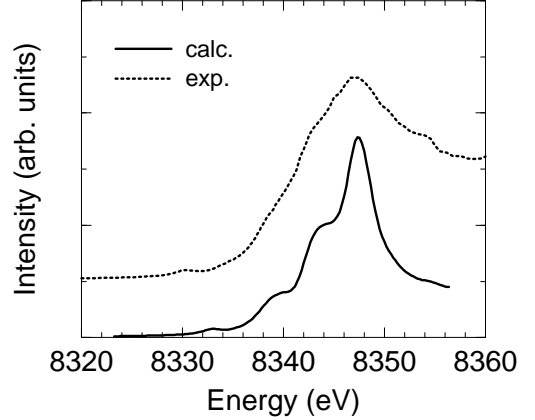


FIG. 4: Absorption coefficient  $A(\omega)$  around the  $K$  edge and the experimental fluorescence spectrum (Ref. 5). The core-hole energy was adjusted such that the peak position coincided with that in the experiment.

##### B. Magnetic RXS spectra

We evaluate the nonresonant term using the “spherical approximation” and “dipolar approximation” for the Fourier transforms  $\mathbf{S}(\mathbf{G})$  and  $\mathbf{L}(\mathbf{G})$ , respectively<sup>32</sup>.  $\mathbf{S}(\mathbf{G})$  is expressed as

$$\mathbf{S}(\mathbf{G}) \approx \frac{1}{\sqrt{N}} \sum_n e^{-i\mathbf{G} \cdot \mathbf{R}_n} \langle j_{0n} \rangle \langle \mathbf{S}_n \rangle, \quad (12)$$

with

$$\langle j_{0n} \rangle = \int_0^{R_{\text{MT}}} j_0(Gr) [\phi_{nl}(r)]^2 r^2 dr, \quad (13)$$

where  $j_0(x) = \sin x/x$ .  $R_{\text{MT}}$  is the MT radius and  $\phi_{nl}(r)$  is the radial function with  $l$  being the angular momentum on the Ni  $n$  site.  $\langle \mathbf{S}_n \rangle$  is the average of the spin operator within the MT sphere at site  $n$ . The  $3d$  states ( $l = 2$ ) give a dominant contribution.

$\mathbf{L}(\mathbf{G})$  is expressed as

$$\mathbf{L}(\mathbf{G}) \approx \frac{1}{\sqrt{N}} \sum_n e^{-i\mathbf{G} \cdot \mathbf{R}_n} \langle g_{0n} \rangle \langle \mathbf{L}_n \rangle, \quad (14)$$

with

$$\langle g_{0n} \rangle = \int_0^{R_{\text{MT}}} g_0(Gr) [\phi_{nl}(r)]^2 r^2 dr, \quad (15)$$

where  $g_0(x) = \frac{2}{x^2}(1 - \cos x)$ .  $\langle \mathbf{L}_n \rangle$  is the average of the angular momentum with respect to the angular part of the wave function within the MT sphere at the Ni  $n$  site. Again, the  $3d$  states give the dominant contribution. Figure 5 shows calculated  $|\mathbf{S}(\mathbf{G})|/\sqrt{N}$  and  $|\mathbf{L}(\mathbf{G})|/\sqrt{N}$  and those in the experiment<sup>3</sup>. The calculated values are slightly smaller than the experimental ones. This is because the LDA calculation underestimates the magnetic moments. The Fourier transform  $\mathbf{S}(\mathbf{G})$  can be directly evaluated without the spherical approximation from the LDA wavefunctions. We compare the results with those evaluated from the spherical approximation. The values in units of  $\hbar$  are  $|\mathbf{S}(\mathbf{G})|/\sqrt{N} = 0.57(0.56)$ ,  $0.32(0.33)$ , and  $0.10(0.13)$  for  $\mathbf{G} = (\frac{1}{2}\frac{1}{2}\frac{1}{2})$ ,  $(\frac{3}{2}\frac{3}{2}\frac{3}{2})$ , and  $(\frac{5}{2}\frac{5}{2}\frac{5}{2})$ , respectively, where the numbers in parentheses are values obtained by the spherical approximation. The spherical approximation works rather well for small values of  $|\mathbf{G}|$ . A similar tendency is expected to exist for  $\mathbf{L}(\mathbf{G})$  calculated with the dipolar approximation, according to the study for  $\text{Ni}^{++}$  by Blume.<sup>33</sup>

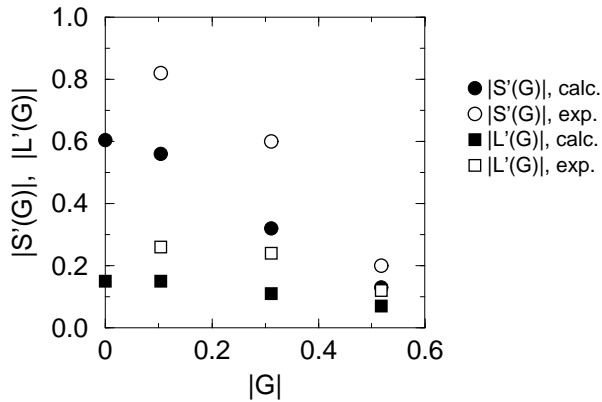


FIG. 5: Form factors of the spin and orbital moments. Circles: the spin moment per Ni site,  $|\mathbf{S}'(\mathbf{G})| \equiv |\mathbf{S}(\mathbf{G})|/\sqrt{N}$ . Squares: the orbital moment per Ni site,  $|\mathbf{L}'(\mathbf{G})| \equiv |\mathbf{L}(\mathbf{G})|/\sqrt{N}$ .

Once  $\mathbf{S}(\mathbf{G})$  and  $\mathbf{L}(\mathbf{G})$  are obtained, the nonresonant contribution is easily evaluated. Then the resonant contribution is evaluated by replacing the intermediate state  $|\Lambda\rangle$  in Eq. (3.8) and  $|\Lambda'\rangle$  in Eq. (3.11) with the unoccupied  $p$  and  $d$  symmetric states given by the band-structure calculation. We confine ourselves to the calculation on a single domain of  $\mathbf{S}_1$  with the AF modulation vector  $\mathbf{Q}$  fixed at  $(\frac{1}{2}\frac{1}{2}\frac{1}{2})$ . Figure 6(a) shows the spectra in the  $\sigma \rightarrow \pi'$  channel for  $\mathbf{G} = (\frac{1}{2}\frac{1}{2}\frac{1}{2})$  as a function of photon energy. The lower panel of Fig. 6(a) shows the calculated spectra at the azimuthal angle  $\psi = 270^\circ$ , where  $\psi$  is defined such that the scattering plane at  $\psi = 0$  contains the  $[1, -1, 0]$  crystal axis. The core-hole energy has

already been determined such that the calculated peak in the  $K$ -edge absorption coefficient coincides with the experimental one. The upper panel of Fig. 6(a) shows the experimental curve at  $\psi = 0^\circ$ , where the absorption correction is made.<sup>17</sup> The experiment is carried out on a sample in which three domains of  $\mathbf{S}_1$ ,  $\mathbf{S}_2$ , and  $\mathbf{S}_3$  are mixed with various relative volumes.

We obtain several peaks at around  $\hbar\omega = 8347$  eV due to the E1 transition. The calculated curve agrees well with the experimental one. Such comparison makes sense, because the spectral shape is a function of photon energy and depends little on domains and azimuthal angle.<sup>34</sup> The E1 intensity arises from the orbital polarization in the  $4p$  states. To clarify how the polarization is induced, we calculate the spectra by turning the SOI on and off separately on the  $3d$  states and on the  $4p$  states. The results are shown in the upper panel of Fig. 6(b). The former slightly suppresses the E1 intensity, while the latter does so strongly. This indicates that, for the  $4p$  orbital polarization, the contribution of the  $3d$  orbital polarization through the  $p$ - $d$  hybridization is quite small and the  $4p$  orbital polarization is mainly induced by the  $4p$  spin polarization through the SOI. This is consistent with the recent analysis of the  $K$ -edge MCD in the ferromagnetic phase of  $\text{Mn}_3\text{GaC}$  (Ref. 16) where it was clarified that the  $4p$  orbital polarization near the Fermi level is mainly induced by coupling to the  $3d$  orbital polarization, while that away from the Fermi level is induced by the  $4p$  spin polarization through the SOI.

In addition to the main-edge peak, we obtain another peak at around  $\hbar\omega = 8333$  eV. This pre-edge intensity is attributed to the E2 transition, that is, the transition to unoccupied  $3d$  states in the intermediate state. As shown in the upper panel of Fig. 6(b), partially turning the SOI off generates small E1 intensities around  $\hbar\omega = 8333$  eV, but the net contribution from the E1 transition (the solid line in the upper panel of Fig. 6(b)) becomes negligible due to a cancellation. As shown in the lower panel of Fig. 6(b), the E2 intensity is strongly suppressed by turning the SOI off on the  $3d$  states, indicating that it originates from the  $3d$  orbital polarization. The magnitude of the pre-edge peak is rather small compared to that of the main-edge peak, though the  $3d$  orbital polarization is much larger than the  $4p$  orbital polarization. The experimental pre-edge peak is located at  $\hbar\omega = 8330$  eV, which is 3 eV lower than the calculated position. We can attribute this difference to the effect of the interaction between the core hole and the  $3d$  states. The attractive interaction is expected to be stronger on the  $3d$  states than on the  $4p$  states, because the former states are more localized than the latter ones. The nonresonant contribution is extremely small at this azimuthal angle.

In Fig. 7, we show the RXS spectra calculated with the LDA and the LDA+ $U$ . The intensity is enhanced due to the local Coulomb interaction  $U_{\text{eff}}$ . This is consistent with the enhancement of the orbital moment (see Table I). The pre-edge peak is shifted to higher energy on introducing  $U_{\text{eff}}$ , which correlates with the opening

larger energy gap. Nevertheless, the effect of  $U_{\text{eff}}$  on the whole spectral shape is small.

Figure 8 shows the spectra in the  $\sigma \rightarrow \sigma'$  channel for  $\mathbf{G} = (\frac{1}{2}\frac{1}{2}\frac{1}{2})$ . Both the calculated and experimental curves are for  $\psi = 0$ . The absorption correction is not made on the experimental curve, so the nonresonant intensities below and above the resonant peak are not the same in the experimental curve<sup>5</sup>. Since the E1 transition is forbidden for all  $\psi$  in the  $\sigma \rightarrow \sigma'$  channel, no main-edge peak appears. The pre-edge peak is located at an  $\sim 3$  eV higher position, due to the same reason as in the case of the  $\sigma \rightarrow \pi'$  channel. We obtain a Fano-type antiresonant dip on the low-energy side of the peak, which arises from an interference with the nonresonant contribution, in agreement with the experiment.

Finally we calculate the azimuthal-angle dependence of the intensity. Although the calculation is performed for a single domain and it cannot be directly compared with the experimental results, it may serve as a guide for analyzing mixed domains. Figure 9 shows the result for  $\mathbf{G} = (\frac{1}{2}\frac{1}{2}\frac{1}{2})$ . The upper (lower) panel shows the intensity of the main-edge (pre-edge) peak at  $\hbar\omega = 8347$  eV (8333 eV). The dependence of the main-edge peak is controlled by the geometrical factor of the E1 transition. As already mentioned, the E1 transition is completely forbidden in the  $\sigma \rightarrow \sigma'$  channel.

## V. CONCLUDING REMARKS

We presented a theoretical study of the magnetic RXS around the  $K$  edge of Ni in antiferromagnetic NiO using the FLAPW band-structure calculation in the density-functional theory. The calculation reproduced the experimental spectra, thus demonstrating the usefulness of the *ab-initio* calculation. The main-edge peak originates from the orbital polarization in the  $4p$  states through the E1 transition. We found that the  $4p$  orbital polarization is mainly generated from the  $4p$  spin polarization through the SOI and the effect of coupling to the  $3d$  orbital polarization at neighboring Ni sites is found to be quite small.

The  $4p$  orbital polarization is closely related to the  $K$ -edge MCD spectra. It is known from the analysis of the MCD spectra in  $\text{Mn}_3\text{GaC}$  (Ref. 16), and in Fe, Co and Ni (Ref. 12) that the MCD signals near the Fermi level are generated mainly by the  $4p$  orbital polarization coupled to the  $3d$  orbital polarization at neighboring sites, while the MCD signals well above the Fermi level are generated from the  $4p$  orbital polarization coupled to the  $4p$  spin polarization through the SOI. The present finding for the main-edge peak is corresponding to the latter.

We also obtained the pre-edge intensity through the E2 transition. The contribution of the E1 transition to the pre-edge intensity is found to be negligible. This shows a contrast with the RXS spectra as to the orbital-ordering spots in  $\text{LaMnO}_3$ . The E1 transition generates pre-edge intensity through mixing  $4p$  states with neighboring  $3d$  states. In  $\text{LaMnO}_3$  the pre-edge intensity of the E1 transition is much smaller than the main-edge intensity but still larger than the pre-edge intensity of the E2 transition. In the present case, the main-edge intensity on the magnetic spot is much smaller than that on the orbital-ordering spot in  $\text{LaMnO}_3$ , and so becomes the pre-edge intensity of the E1 transition. Thereby the intensity of the E2 transition becomes relatively large.

The calculated pre-edge peak position relative to the main-edge peak is  $\sim 3$  eV higher than the experimental one. This suggests that the core-hole potential is more effective on the  $3d$  states. The inclusion of such an effect by extending the calculation scheme is left for future studies.

## Acknowledgments

We have used the FLAPW code developed by Professor N. Hamada. We thank him for allowing us to use his code. We would also like to thank Dr. W. Neubeck for sending us his thesis and for valuable discussion. This work was partially supported by a Grant-in-Aid for Scientific Research from the Ministry of Education, Science, Sports and Culture, Japan.

<sup>1</sup> A. Stunault, F. de Bergevin, D. Wermeille, C. Vettier, T. Brückel, N. Bernhoeft, G. J. McIntyre, and J. Y. Henry, Phys. Rev. B **60**, 10170 (1999).

<sup>2</sup> R. Caciuffo, L. Paolasini, A. Sollier, P. Ghigna, E. Pavarini, J. van den Brink, and M. Altarelli, Phys. Rev. B **65**, 174425 (2002).

<sup>3</sup> W. Neubeck, C. Vettier, K.-B. Lee, and F. de Bergevin, Phys. Rev. B **60**, R9912 (1999).

<sup>4</sup> J. P. Hill, C.-C. Kao, and D. F. McMorrow, Phys. Rev. B **55**, R8662 (1997).

<sup>5</sup> W. Neubeck, C. Vettier, F. de Bergevin, F. Yakhov, D. Mannix, O. Bengone, M. Alouani, and A. Barbier, Phys. Rev. B **63**, 134430 (2001).

<sup>6</sup> Y. Murakami, J. P. Hill, D. Gibbs, M. Blume, I. Koyama,

M. Tanaka, H. Kawata, T. Arima, Y. Tokura, K. Hirota, et al., Phys. Rev. Lett. **81**, 582 (1998).

<sup>7</sup> S. Ishihara and S. Maekawa, Phys. Rev. Lett. **80**, 3799 (1998).

<sup>8</sup> I. S. Elfimov, V. I. Anisimov, and G. Sawatzky, Phys. Rev. Lett. **82**, 4264 (1999).

<sup>9</sup> M. Benfatto, Y. Joly, and C. R. Natori, Phys. Rev. Lett. **83**, 636 (1999).

<sup>10</sup> M. Takahashi, J. Igarashi, and P. Fulde, J. Phys. Soc. Jpn. **68**, 2530 (1999).

<sup>11</sup> J. Igarashi and M. Takahashi, Phys. Rev. B **63**, 184430 (2001).

<sup>12</sup> G. Schütz, W. Wagner, W. Wilhelm, P. Kienle, R. Zeller, R. Frahn, and G. Materlik, Phys. Rev. Lett. **58**, 737 (1987).

- <sup>13</sup> H. Ebert, P. Strange, and B. L. Gyorffy, J. Appl. Phys. **63**, 3055 (1988).
- <sup>14</sup> J. Igarashi and K. Hirai, Phys. Rev. B **50**, 17820 (1996).
- <sup>15</sup> M. Takahashi, M. Usuda, and J. Igarashi, Phys. Rev. B **67**, 064425 (2003).
- <sup>16</sup> M. Takahashi and J. Igarashi, Phys. Rev. B **67**, 245104 (2003).
- <sup>17</sup> W. Neubeck, Ph.D. thesis, Joseph Fourier University, Grenoble I (2000).
- <sup>18</sup> T. Takeda and J. Kübler, J. Phys. F Met. Phys. **9**, 661 (1979).
- <sup>19</sup> H. J. F. Jansen and A. J. Freeman, Phys. Rev. B **30**, 561 (1984).
- <sup>20</sup> S. H. Vosko, L. Wilk, and M. Nusair, Can. J. Phys. **58**, 1200 (1980).
- <sup>21</sup> V. I. Anisimov, F. Aryasetiawan, and A. I. Lichtenstein, J. Phys: Condens. Matter **9**, 767 (1997).
- <sup>22</sup> I. Solov'yev, N. Hamada, and K. Terakura, Phys. Rev. B **53**, 7158 (1996).
- <sup>23</sup> V. Fernandez, C. Vettier, F. de Bergevin, C. Giles, and W. Neubeck, Phys. Rev. B **57**, 7870 (1998).
- <sup>24</sup> G. A. Sawatzky and J. W. Allen, Phys. Rev. Lett. **53**, 2339 (1984).
- <sup>25</sup> A. K. Cheetham and D. A. O. Hope, Phys. Rev. B **27**, 6964 (1983).
- <sup>26</sup> E. Arola, P. Strange, and B. L. Gyorffy, Phys. Rev. B **55**, 472 (1997).
- <sup>27</sup> P. Rennert, Phys. Rev. B **48**, 13559 (1993).
- <sup>28</sup> P. Rennert, J. Appl. Phys. **76**, 6459 (1994).
- <sup>29</sup> F. de Bergevin and M. Brunel, Acta Crystallogr., Sect. A: Cryst. Phys., Diffr., Theor. Gen. Crystallogr. **37**, 324 (1981).
- <sup>30</sup> M. Blume, J. Appl. Phys. **57**, 3615 (1985).
- <sup>31</sup> M. Blume and D. Gibbs, Phys. Rev. B **37**, 1779 (1988).
- <sup>32</sup> P. Coppens, Z. Su, and P. J. Becker, *International Tables for Crystallography* edited by A. J. C. Willson and E. Prince (Kluwer Academic, BOSTON, 1999), vol. C, chap. Analysis of charge and spin densities, pp. 706–727, 2nd ed.
- <sup>33</sup> M. Blume, Phys. Rev. **124**, 96 (1961).
- <sup>34</sup> The relative intensities among the nonresonant term, the E1 transition term, and the E2 transition term depend sensitively on the domains and the azimuthal angle.

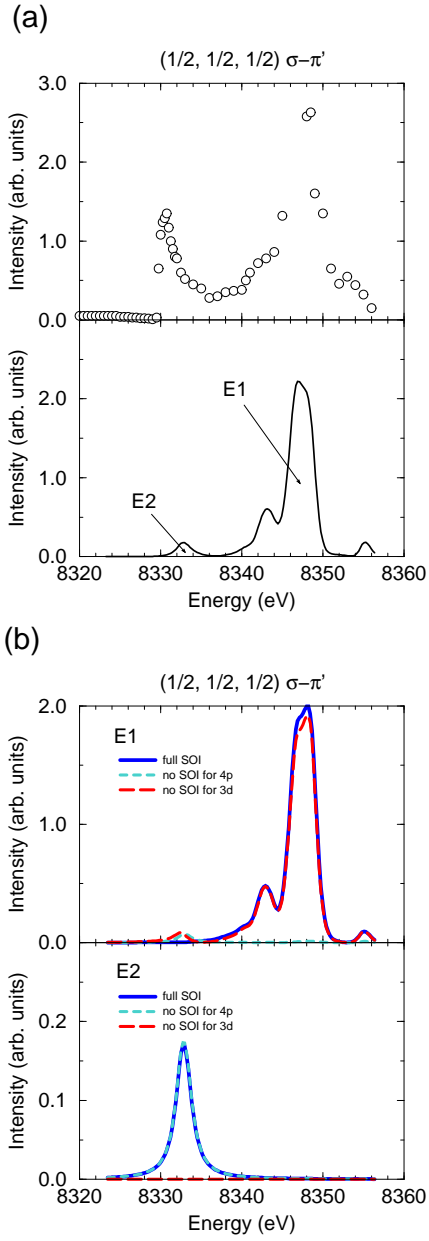


FIG. 6: (color online) (a) Magnetic scattering spectra in the  $\sigma \rightarrow \pi'$  channel for  $\mathbf{G} = (\frac{1}{2}, \frac{1}{2}, \frac{1}{2})$ , as a function of photon energy. The upper panel shows the experimental spectrum at  $\psi = 0^\circ$  with three domains mixed and the absorption correction is performed.<sup>17</sup> The lower panel shows the calculated spectrum at  $\psi = 270^\circ$  for the domain of  $\mathbf{S}_1$ . Resonant E1, E2, and nonresonant contributions are included in this calculation. (b) Magnetic scattering spectra by turning the SOI off separately on the 3d states and the 4p states, respectively. Nonresonant contribution is not included in these spectra.



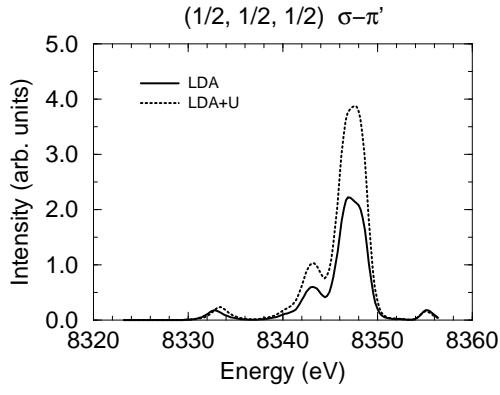


FIG. 7: Comparison between the RXS spectra calculated by the LDA (solid line) and the LDA+ $U$  with  $U_{\text{eff}} = 2$  eV (dashed line).

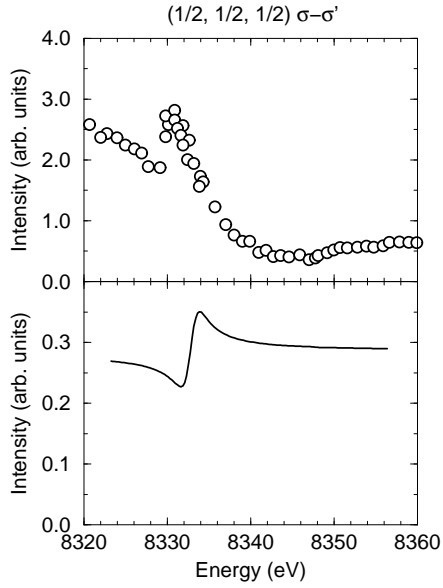


FIG. 8: Magnetic scattering spectra in the  $\sigma \rightarrow \sigma'$  channel for  $\mathbf{G} = (\frac{1}{2}, \frac{1}{2}, \frac{1}{2})$ , as a function of photon energy. The upper panel shows the experimental spectra at  $\psi = 0$  without absorption correction.<sup>5</sup> The lower panel shows the calculated results at  $\psi = 0$ .

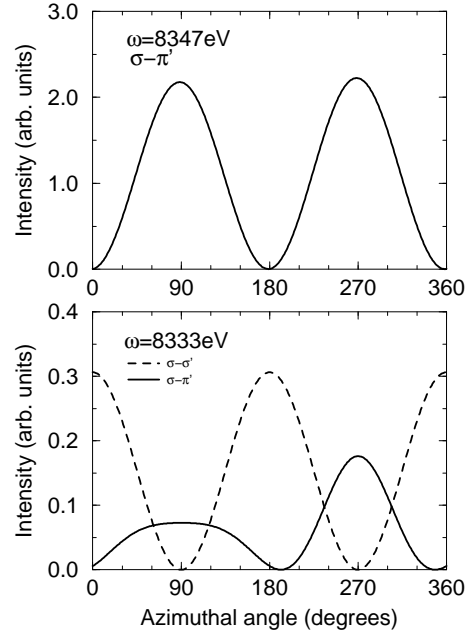


FIG. 9: Azimuthal-angle dependence of the magnetic scattering intensity for  $\mathbf{G} = (\frac{1}{2} \frac{1}{2} \frac{1}{2})$ . The upper panel is for the pre-edge peak at 8333 eV (non-resonant contribution is eliminated). The lower panel is for the main peak at 8347 eV.